The unsteady motion of a sphere in a viscoelastic fluid

Becker, L.E.; McKinley, G. H.; Rasmussen, Henrik K.; Hassager, Ole

Published in:
Journal of Rheology

Link to article, DOI:
10.1122/1.550519

Publication date:
1994

Document Version
Publisher's PDF, also known as Version of record

The unsteady motion of a sphere in a viscoelastic fluid

L. E. Becker and G. H. McKinley

Division of Applied Sciences, Harvard University, Cambridge, Massachusetts 02138

H. K. Rasmussen and O. Hassager

Institut for Kemiteknik, Technical University of Denmark (DTH), Denmark

(Received 5 April 1993; accepted 10 September 1993)

Synopsis

The motion of a sphere accelerating from rest along the center line of a cylindrical tube filled with a polyisobutylene (PIB) Boger fluid is examined both experimentally, using a digital imaging system, and numerically via a Lagrangian finite element method for single and multimode Oldroyd models including inertia. Spheres of diameter 2.54 cm and varying densities are released in a tube of radius 5.23 cm. Deborah numbers in the range $0.4 \leqslant De \leqslant 11.7$ are obtained, and the experimental results show transient velocity overshoots of up to 50% before the spheres approach their final constant settling velocity. Independent measurements of this settling velocity indicate significant drag increases at high De. The numerical calculations are compared with the experimental data, and markedly improved agreement is obtained for multimode simulations.

I. INTRODUCTION

The motion of a sphere through a quiescent fluid is one of the classic problems in Newtonian fluid mechanics, and the corresponding behavior in non-Newtonian liquids is the focus of much current research. The fluid motion near the sphere is inhomogeneous, with strong extensional velocity gradients near the fore and aft stagnation points, and large shearing components near the equator of the sphere. For such reasons, the falling ball viscometer has frequently been suggested as an instrument for obtaining information about the material functions of a non-Newtonian fluid in a nonhomogeneous flow (see, e.g., Cygan and Caswell, 1971; Cho *et al.*, 1984). The steady motion of a sphere in a cylindrical tube containing viscoelastic fluid has also been selected as a benchmark problem for the evaluation of numerical codes (Hassager, 1988). A large body of experimental and numerical data concerning the steady motion of spheres in viscoelastic fluids has been published over the past 15 years, and detailed reviews have been published elsewhere (Walters and Tanner, 1992; Chhabra, 1992).

In this work, we study the time-dependent motion of a sphere along the center line of a cylindrical tube containing viscoelastic fluid as it accelerates from rest under the influence of gravity. Early theoretical work for such transient motion of a sphere in an unbounded domain was performed by King and Waters (1972) using the linear vis-

coelastic Jeffreys model coupled with the time-dependent form of the equations of motion for creeping flow. Analytic solutions for the time-dependent velocity of the sphere were obtained, and the results showed velocity overshoots together with the possibility of damped oscillations about the ultimate steady-state settling velocity U_∞ depending upon the value of two dimensionless groups. These groups can be interpreted as the elasticity number

$$E = \frac{\lambda_1 \eta_0}{2a^2 \rho_f}, \tag{1}$$

and the ratio of the retardation time to the relaxation time

$$\beta = \frac{\lambda_2}{\lambda_1} = \frac{\eta_s}{\eta_0}, \tag{2}$$

where a is the radius of the sphere, ρ_f is the fluid density, η_0 is the zero-shear-rate viscosity of the fluid, and η_s is the solvent viscosity. The elasticity number E is usually interpreted in steady flows as the ratio of elastic stresses ($\sim \lambda_1 \eta_0 U_\infty^2 / a^2$) to inertial stresses ($\sim \rho_f U_\infty^2$) in the fluid. In transient motions, however, it is more useful to consider E as the ratio of the elastic time scale ($\sim \lambda_1$) for growth of viscoelastic stresses in the flow to the viscous time scale ($\sim \rho_f a^2 / \eta_0$) for diffusion of vorticity information from the accelerating sphere into the surrounding fluid.

Lai (1974, 1978) solved the same problem for the time-dependent drag on the sphere given a prescribed velocity profile. More recently, Ramkissoon and Shifang (1993) determined analytically the flow field in the surrounding fluid due to the unsteady motion of a sphere through a second-order fluid.

This problem has also been adopted recently as a model geometry for testing transient numerical algorithms. Zheng and Phan-Thien (1992) used a boundary element method to generate numerical solutions for the transient motion of a sphere in an upper-convected Maxwell model, including the presence of the cylindrical tube walls, but ignoring the inertia of the fluid. They found that increasing the dimensionless geometric ratio

$$\kappa = \frac{a}{R}, \tag{3}$$

where a is the radius of the sphere and R is the radius of the tube, led to a decrease in amplitude of the velocity overshoots, and to an increase in frequency of the oscillations at a fixed Deborah number.

Bodart and Crochet (1993) provide similar computations using the Oldroyd-B model including the effects of fluid inertia and the constraining presence of the tube walls. In this work, they show that for a sphere of fixed radius and density, increasing κ leads to an increase in the *relative* magnitude of the velocity overshoot with respect to the ultimate asymptotic settling velocity U_∞.

However, on the experimental side, almost no data are available for this transient problem. A qualitative strobe photograph is given by Walters and Tanner (1992) for a 3.2 cm diameter sphere accelerating from rest in a narrow tube containing Boger fluid. The photograph indicates that the sphere overshoots its ultimate steady settling velocity by about 300%. The present study uses a digital imaging system to provide quantitative measurements of the transient velocity of a sphere with high spatial and temporal resolution, and these results are compared with Lagrangian finite element

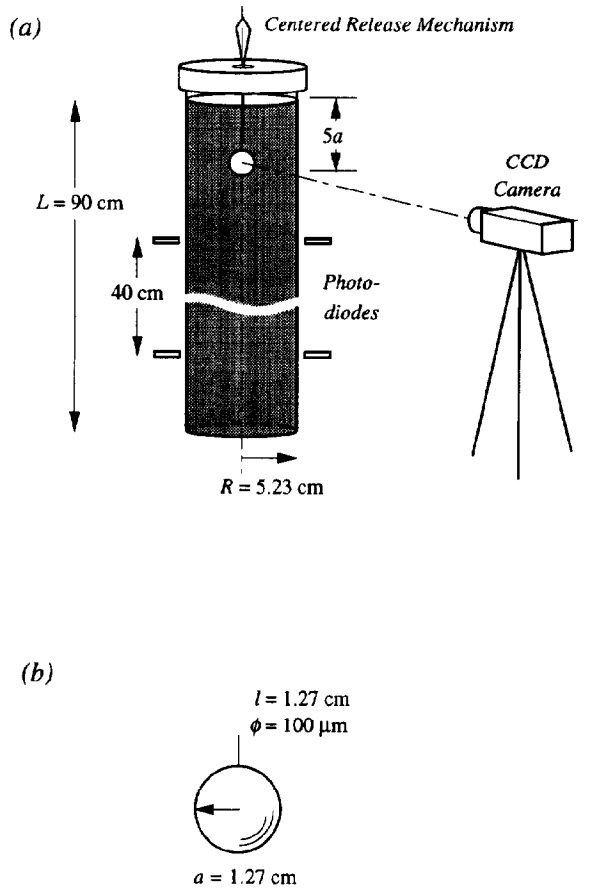

FIG. 1. (a) Schematic diagram of the experimental apparatus for measuring transient and steady motion of a sphere falling through a viscoelastic fluid. (b) Detail of the sphere and attached wire release mechanism.

calculations using both single and multimode formulations of the Oldroyd-B model, incorporating both inertia and the presence of the tube walls.

II. EXPERIMENTAL TECHNIQUE

A. Overview

The overall experiment is shown in Fig. 1(a). A 90 cm long plexiglass cylinder of internal radius $R = 5.23$ cm is filled with Boger fluid, and its axis is carefully aligned parallel with gravity. Although not shown in Fig. 1(a), the entire cylinder is enclosed in a rectangular box filled with refractive-index matched fluid to eliminate refraction effects at the curved air–cylinder interface. The infrared photodiodes are used to obtain an independent estimate of the ultimate steady-state settling velocity U_∞ of each sphere by measuring the transient time through a 40 cm section of the tube. This section was located 30 cm ($24a$) below the free surface and 20 cm ($16a$) above the closed end of the cylindrical tube, in order to ensure that initial transients and end effects do not affect the measurements.

TABLE I. The densities ρ_s of the spheres used in the experimental measurements, and the nominal values of the Deborah number and Reynolds number estimated *a priori* using the settling velocity U_s expected in a Newtonian fluid of equivalent viscosity.

Material	ρ_s(g/cm^3)	U_s (cm/s)	De	Re
Delrin	1.38	0.649	0.406	0.011
Teflon	2.18	1.71	1.07	0.028
Ceramic	3.85	3.91	2.45	0.064
Bronze	7.57	8.84	5.53	0.145
Chrome steel	7.81	9.16	5.73	0.150
Tungsten carbide	15.0	18.7	11.7	0.307

Since we are interested in resolving the initial transient acceleration of the sphere from rest, great attention was paid to the design of the release mechanism of the sphere. In our numerical simulations, gravity is essentially turned on instantaneously at time $t = 0$; however, such a system is not realizable experimentally. Preliminary experiments showed that the presence of any solid bounding surface (e.g., electromagnets, tweezers, clamps, etc.) near the stationary sphere resulted in a delayed initial acceleration of the sphere due to the high lubrication forces that develop in the thin layer of viscous fluid entering the gap between the sphere and its mounting device. These effects were eliminated by using the configuration shown in Fig. 1(b). A 1.27 cm piece of 100 μm diameter wire is attached to a high tolerance 2.54 cm diameter sphere, and the free end of the wire is then gripped by a pair of long, thin tweezers. The tweezers are partially immersed in the fluid and carefully aligned with the center line of the tube, with the center of the sphere being 5 sphere radii below the free surface. The steady creeping motion of a Newtonian fluid past a sphere attached to a slender body was studied by DeMestre and Katz (1974) for an unbounded domain, and based on that analysis, the additional drag arising from the thin wire is calculated to reduce our measurements of the ultimate steady-state settling velocity of the sphere by no more than 2%–3%. This correction is of approximately the same size as our experimental error. Comparisons of the drag enhancement experimentally observed in the viscoelastic fluid using spheres with and without the string attached also showed no statistically significant difference in the calculated drag coefficients. The wire is not included in the simulations presented here. However, the simulations do show very strong gradients in polymer configuration near the aft stagnation point, and the wire may need to be included in future simulations, especially if the stability of the flow is to be considered.

The various spheres used in these experiments were commercially available ball bearings of diameter 2.54 cm and sphericity tolerances of less than 2.5 μm. The density ρ_s of these spheres is shown in Table I, together with the steady Newtonian settling velocity U_s expected for each sphere in a tube of equal radius filled with a viscous Newtonian solvent of equivalent viscosity η_0. This velocity is calculated by equating the gravitational body force on the sphere with the viscous drag exerted on a sphere in a tube as

$$U_s = \frac{(4/3)\pi a^3(\rho_s - \rho_f)g}{6\pi\eta_0 a K_N}, \tag{4}$$

where g is the gravitational acceleration and $K_N(\kappa)$ is the Faxen wall correction factor [Happel and Brenner (1983)] describing the reduction in velocity resulting from the

presence of walls. For $\kappa = 0.243$, the correction factor is $K_N = 1.93$. As the radius of the tube increases and the constraining effect of the wall decreases, $\kappa \to 0$ and $K_N \to 1$, so that Eq. (4) reduces to the well-known Stokes settling velocity.

We also wish to compare our results with transient numerical simulations; however, the relevant dimensionless quantities measuring the importance of viscous, inertial, and elastic effects in the steady flow ultimately achieved are unknown *a priori*. For this reason, we choose to define *nominal* Reynolds numbers and Deborah numbers in terms of the settling velocity U_s expected for such a sphere as

$$\mathrm{Re} = \frac{2a\rho_f U_s}{\eta_0} \tag{5}$$

and

$$\mathrm{De} = \frac{\lambda_1 U_s}{a}, \tag{6}$$

respectively. It should be noted that the elasticity number E defined in Eq. (1) is simply the ratio of De to Re, and is independent of the flow kinematics, depending only upon the geometry and the material functions of the fluid. For the PIB Boger fluid used in this work, with the viscometric properties given in Sec. II B, the elasticity number $E = 38.1$, indicating that the viscoelastic stresses acting on the sphere grow on a time scale much longer than that required for diffusion of vorticity information.

The values of De and Re shown in Table I thus represent the range of parameters expected if the viscosity of the non-Newtonian fluid is not a function of the velocity gradients in the flow, and if the wall correction factor K is not a function of De or Re. This former assumption is valid over a wide range of shear rates for the Boger fluid, however, in general the second assumption is incorrect.

Numerous experimental investigations, most recently those of Mena *et al.* (1987) and Chhabra and Uhlherr (1988), have investigated the steady motion of spheres in Boger fluids. Most of these investigations refer to Reynolds and Deborah numbers based on the steady sphere velocity U_∞. We refer to these as the *actual* Reynolds and Deborah numbers, and denote them De_1 and Re_1, respectively. Also for steady motion it is customary to define a drag correction factor K (κ, De_1) as follows:

$$K = \frac{F_{\mathrm{drag}}}{6\pi\eta a U_\infty} = \frac{(4/3)\pi a^3(\rho_s - \rho_f)g}{6\pi\eta a U_\infty}. \tag{7}$$

Then the nominal and actual Reynolds and Deborah numbers are related to one another as follows:

$$\mathrm{Re}_1 = \frac{2a\rho_f U_\infty}{\eta_0} = \mathrm{Re}\,\frac{K_N(\kappa)}{K(\kappa,\mathrm{De}_1)}, \tag{8}$$

$$\mathrm{De}_1 = \frac{\lambda_1 U_\infty}{a} = \mathrm{De}\,\frac{K_N(\kappa)}{K(\kappa,\mathrm{De}_1)}. \tag{9}$$

In general, for values of $\kappa < 0.3$, the correction factor is only weakly dependent on fluid elasticity, and K varies by less than 20%. The values of De and Re in Table I thus provide reasonable *a priori* estimates of the large Deborah numbers that can be achieved in this flow.

B. Fluid rheology

The test fluid used in these experiments is a Boger fluid composed of 0.31 wt.% polyisobutylene (PIB), 4.83 wt.% tetradecane (C14), and 94.86 wt.% polybutene (PB), and it has been extensively characterized over a range of temperatures in steady and transient shear flows (see Quinzani *et al.*, 1990). The zero-shear-rate viscometric properties have been determined as $\eta_0 = 13.76$ Pa s, $\eta_s = 8.12$ Pa s, and $\Psi_{10} = 8.96$ Pa s^2, where Ψ_{10} is the first normal stress coefficient in the limit of zero shear rate. Fitting these values to the predictions of the Oldroyd-B model in steady shear flow yields a relaxation time $\lambda_1 = 0.794$ s and a viscosity ratio $\beta = 0.59$. Due to its simplicity, the Oldroyd-B constitutive equation is frequently used as a model for Boger fluids. Hence we present numerical simulations for the transient sphere motion using an Oldroyd-B single mode model with the above parameters. Although the Oldroyd-B model provides a reasonable description of the material functions for a Boger fluid in steady shearing flows, it is widely appreciated that the presence of a single relaxation time λ_1 renders the model incapable of quantitatively describing transient phenomena of real polymeric fluids even in the linear viscoelastic limit (Bird *et al.*, 1987). Hence numerical simulations were also performed with a multimode formulation of the Oldroyd-B constitutive equation using a four-mode spectrum of time constants for the Boger fluid, obtained from linear viscoelastic measurements (Quinzani *et al.*, 1990). The relaxation times for modes $i = \{1,...,4\}$ are given by $\lambda_i = \{2.755, 0.7361, 0.1094, 0.0098\}$ s, and the respective viscosities for each mode are $\eta_i = \{1.108, 1.677, 1.657, 1.211\}$ Pa s. The material properties of Boger fluids are highly temperature-dependent, and are accurately described for this fluid by an Arrhenius equation with a flow activation energy of $\Delta H = 61.2$ kJ. All of the results presented in this paper have been corrected to 25 °C, using a shift factor evaluated at the appropriate fluid temperature of each experiment.

C. Image analysis

Video images of the Lagrangian displacement of the sphere are obtained using a high-resolution monochrome CCD camera (COHU 4910), and recorded on a Super-VHS video recorder (Panasonic AG1960). Eight-bit gray-scale images are also obtained in real time using a frame-grabber data acquisition board (Dipix P360) resident on an Intel 486 personal computer. The Dipix board contains a 32 MHz Texas Instruments Digital Signal Processing Chip (TMS320c30), along with 4 Mb of RAM, which allows us to avoid the bus limitations in the PC and to rapidly analyze the images of the sphere as described below.

A typical digitized image consisting of 160×480 pixels is shown in Fig. 2(a), and the corresponding histogram showing the number of pixels with a given gray-scale intensity is given in Fig. 2(b). The gray level varies from 0 (black) to 255 (white), and hence the image is composed of dark background pixels and bright pixels corresponding to the sphere. All the spheres were painted white for improved contrast. Each digital image is then binarized by selecting the threshold value which best separates the sphere from the background, resulting in the image shown in Fig. 2(c). Finally, the centroid of the circular image of the sphere is calculated via the following algorithm:

$$\bar{x} = \frac{\Sigma_i x_i I_i}{\Sigma_i I_i}, \quad \bar{z} = \frac{\Sigma_i z_i I_i}{\Sigma_i I_i}; \quad I \in \{0,1\}, \tag{10}$$

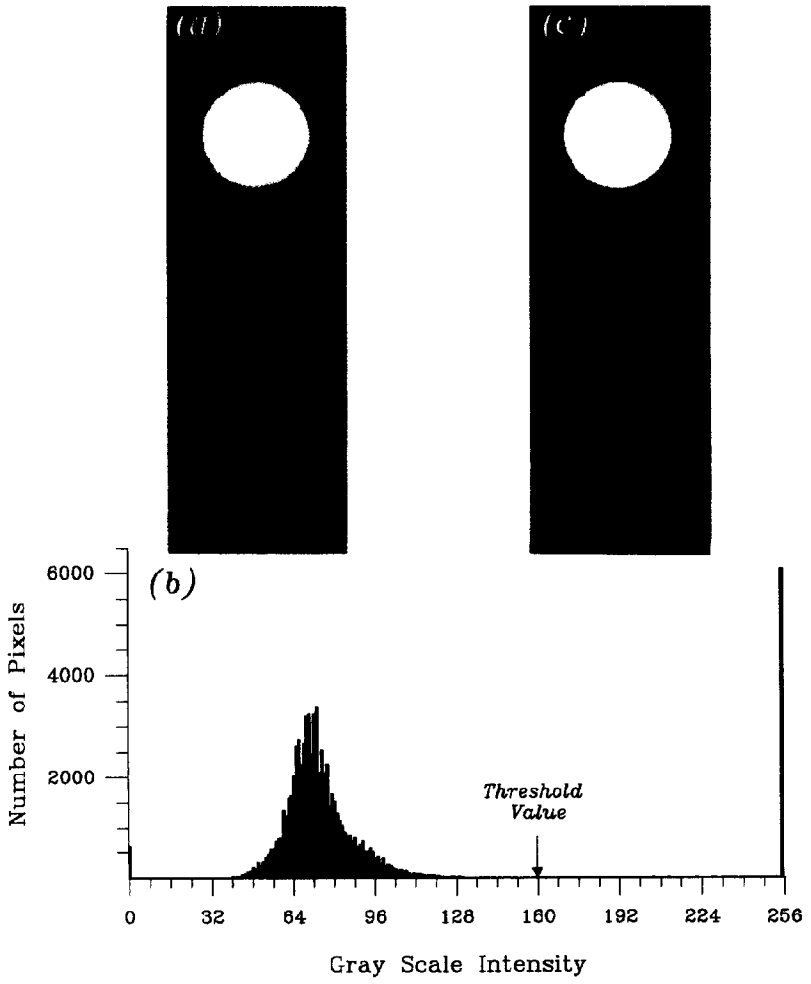

FIG. 2. (a) A typical 8-bit gray-scale image of a 2.54 cm diameter sphere in the tube of Boger fluid. The thin suspending wire is just discernible above the sphere. (b) Histogram of gray-scale intensities for the 76 800 pixels shown in image (a). The sphere corresponds to the large peak with intensities of greater than 250. (c) Binary image of sphere after thresholding image at an intensity of $I = 160$.

where x and z are the coordinates perpendicular to and along the center line of the tube, respectively, and I_i is either 0 or 1 depending on whether pixel i is below or above the threshold, respectively.

Images can be digitized and stored in memory with this system at the NTSC video rate of 30 frames per second. This procedure is used to capture most of the initial transient motion of the released sphere, the images being stored for later post-processing. However, once the memory buffer has been filled to capacity, each new incoming frame is analyzed and subsequently discarded before the next frame is acquired. The time per frame for this process depends on image size; a typical image of approximately 75 000 pixels takes about 0.13 s. This slower process is continued until the sphere leaves the field of view of the camera.

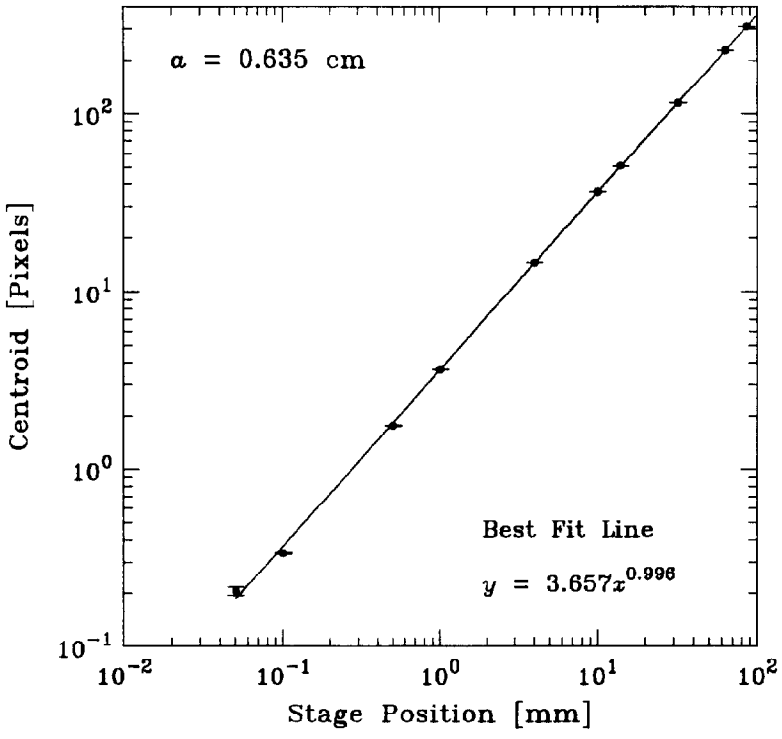

FIG. 3. Calibration curve for determining the accuracy and spatial resolution of the centroid algorithm.

To evaluate the spatial accuracy of our imaging system, the calibration curve shown in Fig. 3 was prepared. A sphere was mounted on a computer-controlled micropositioning stage capable of an absolute positioning accuracy of ± 1 μm, and then displaced by exact spatial increments spanning three orders of magnitude. The centroid of the sphere as obtained via the digital imaging technique is shown on a logarithmic scale against the stage displacement, along with error bars that quickly shrink to a single bar for larger motions. This calibration curve is linear over the entire domain for displacements in the range of 50 μm ($\simeq 0.004a$) to 100 mm ($\simeq 8a$). Calculation of the slope of this curve yields the pixel scale factor for the apparatus.

The overall accuracy of our transient measurements depends on lighting conditions, image distance from the camera, and settling velocity of the sphere. The camera is electronically shuttered to give an exposure time of 2 ms, in order to reduce the blur in the image caused by the motion of the sphere while the shutter is open. At the maximum sphere velocity of $U_s \simeq 19$ cm/s shown in Table I, a shutter speed of 2 ms gives a particle displacement of only 0.38 mm $= 0.03a$. The maximum experimental error in the results including repeatability is $\sim \pm 4$ %.

The Lagrangian coordinates $x_i(t_i)$ and $z_i(t_i)$ of the centroid for a typical experiment are shown in Fig. 4. The abrupt change in the slope of the axial coordinate at $t = 0$ corresponds to the release of the sphere. The dashed line shows the displacement of the sphere expected in a Newtonian fluid obtained by solving the quasisteady Stokes equations and using the Faxen drag correction factor $K_N = 1.93$. It is immediately evident that the slope of the experimental data is initially much steeper than the

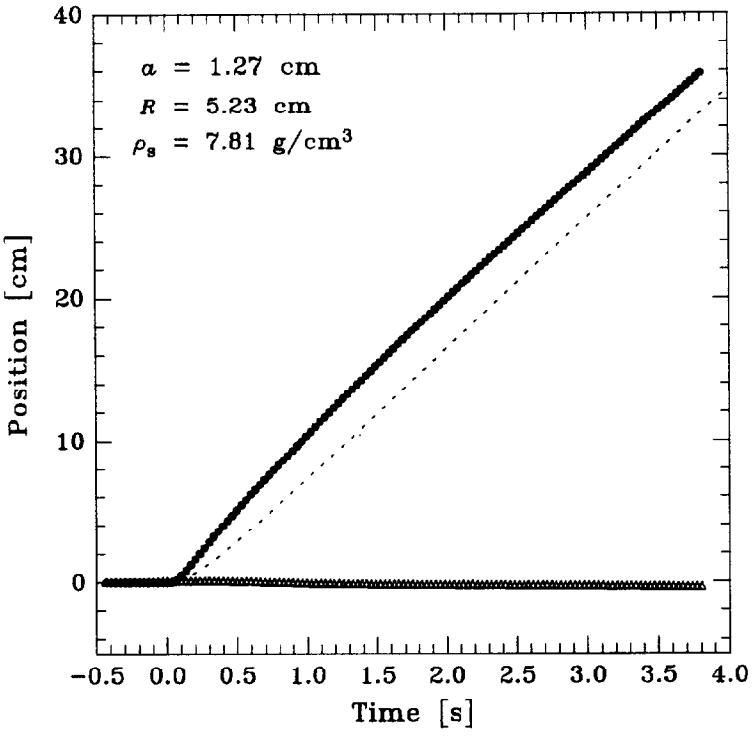

FIG. 4. Centroid coordinates $\{x(t_i),z(t_i)\}$ of a 2.54 cm chrome steel sphere accelerating from rest at time $t = 0$ in the viscoelastic Boger fluid. Solid symbols (●) show the vertical (z) displacement, hollow symbols (△) show the lateral (x) displacement. The dashed line indicates the approximate theoretical Stokes profile.

Newtonian prediction before decreasing at longer times, indicating the presence of an initial velocity overshoot. Careful inspection of the experimental data at long times also shows the ultimate slope is slightly lower than that of the Newtonian prediction, indicating the presence of a drag increase at long times.

Quantitative measurements of the sphere velocity $v_z(t)$ can be obtained by differentiating the position data shown in Fig. 4. In general, differentiation of closely spaced experimental data can lead to the amplification of experimental noise; in this work, we use three-point and five-point centered difference formulas based on Gramm polynomials, as suggested by Whitaker and Pigford (1960). These formulas are given by

$$v_z^{3\text{pt}}(t_i) = \frac{z_{i+1}-z_{i-1}}{2\Delta t} \tag{11}$$

and

$$v_z^{5\text{pt}}(t_i) = \frac{2z_{i+2}+z_{i+1}-z_{i-1}-2z_{i-2}}{10\Delta t}, \tag{12}$$

respectively, where $z_i = z(t_i)$ is the centroid position at time t_i and Δt is the time increment between successive frames. The x coordinate varies only slightly over the course of the experiment, and has a negligible effect on the axial velocities. These formulas minimize the amplification of noise without introducing the excessive

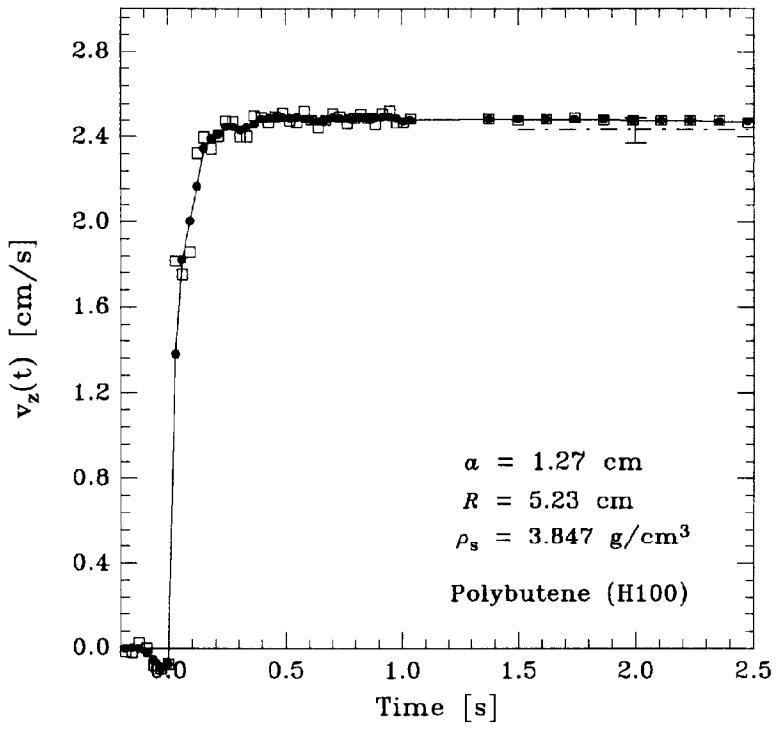

FIG. 5. Transient velocity profile for a ceramic sphere ($\rho_s = 3.85$ g/cm^3) in a viscous Newtonian solvent. (●) Velocity calculated using a five-point difference method: (□) velocity calculated using a three-point difference method.

smoothing associated with spline techniques. However, the formulas do smooth discontinuities in discrete data, such as the physically real discontinuous change in the velocity of the sphere at time $t = 0$. For the first point in the velocity time series where the axial position differs from its initial rest value, a regular two-point forward difference must be used, and the following point at $t_i = 2\Delta t$ is estimated by the three-point formula. At subsequent times, both the three-point and five-point methods are applicable. It was consistently found that while the five-point formula damps out random experimental noise at the expense of temporal resolution, the density of our position-time data was sufficiently high so that real transient phenomena were accurately resolved. Hence, our experimental results have been generated using a five-point difference formula for all but the initial two points. It should also be noted that, with discretely spaced observations of the sphere's position, we can only resolve the initial onset of motion to within $\pm \frac{1}{2} \Delta t$, and our velocity time series should thus be associated with appropriate horizontal error bars.

The results for a test case performed with a 2.54 cm ceramic sphere in a Newtonian solvent of polybutene ($\eta_0 = 22.1$ Pa s) are shown in Fig. 5. As expected, the velocity rises monotonically towards the steady-state value $U_s = 2.43$ cm/s to within the indicated error bars of $\pm 2.5\%$. The inertial time scale associated with acceleration of the sphere is given by $\rho_s a^2/\eta_0 = 26$ ms, and hence the initial transient is barely resolvable with our video camera. Velocity calculations with both three-point and

five-point formulas are shown in the figure, and while their initial estimates differ slightly when velocity gradients are large, they agree well at longer times.

III. NUMERICAL METHOD

In this work, we use a time-dependent Galerkin finite element method based on the Lagrangian kinematic description. A detailed discussion of the basic idea in the method may be found in Rasmussen and Hassager (1993). In the following we present a brief summary of the method, and in particular we demonstrate how inertia and buoyancy are described, since that is not included in Rasmussen and Hassager (1993). In addition, the equation of motion for the sphere is derived, and a refinement with respect to the time integration is presented.

A. Model equations

We use the Lagrangian kinematic specification in a cylindrical coordinate system and let some initial particle positions (r_0, z_0) of the particles at time t_0 be independent variables. The dependent variables are then particle positions (r,z) at the present time t.

The idea is then to follow the flow in time t by solving for the functions $r(r_0,z_0,t)$ and $z(r_0,z_0,t)$ given the initial positions and appropriate boundary conditions for $t > t_0$.

The r and z components of the equations of motion in the Lagrangian form (Lamb, 1932) may be formulated as follows:

$$\rho_f \frac{\partial^2 r}{\partial t^2} + \frac{\partial \mathscr{P}}{\partial r} + \left(\frac{1}{r} \frac{\partial (r\tau_{rr})}{\partial r} - \frac{\tau_{\theta\theta}}{r} + \frac{\partial \tau_{zr}}{\partial z} \right) = 0, \tag{13}$$

$$\rho_f \frac{\partial^2 z}{\partial t^2} + \frac{\partial \mathscr{P}}{\partial z} + \left(\frac{1}{r} \frac{\partial (r\tau_{zr})}{\partial r} + \frac{\partial \tau_{zz}}{\partial z} \right) = 0. \tag{14}$$

The notation for the stresses is that of Bird *et al.* (1987). We let the z axis point upwards, and use the modified pressure $\mathscr{P}$ related to the physical pressure, p by $\mathscr{P} = p + \rho_f g z$.

We use a constitutive relation in which the stress is explicitly split into a (Newtonian) solvent contribution τ_s and a polymer contribution τ_p. The polymer contribution is given by a memory integral over the finite strain tensor $\gamma_{[0]}(r,z,t,t')$ (Bird *et al.*, 1987). Thus we have

$$\tau(r,z,t) = \tau_s(r,z,t) + \tau_p(r,z,t) = -\eta_s \dot{\gamma}(r,z,t) + \int_{-\infty}^{t} M(t-t') \gamma_{[0]}(r,z,t,t') dt'. \tag{15}$$

The memory function is given by

$$M(s) = \sum_{i=1}^{N} \frac{\eta_i}{\lambda_i^2} \exp(-s/\lambda_i), \tag{16}$$

where $s = t - t'$, and $N = 1$ or 4 for the single-mode and multimode models, respectively, as described in Sec. II B.

For later use we also note that the trace of the polymer contribution to the stress is given by

$$\mathrm{tr}(-\tau_p) = \int_{-\infty}^{t} M(t-t')[I_1(r,z,t,t')-3]dt', \tag{17}$$

where I_1 is the first scalar invariant of the Finger strain tensor. We note that $I_1 \geqslant 3$ for all deformations, and that $I_1 = 3$ if and only if there is no deformation. Hence $\mathrm{tr}(-\tau_p)$ as defined here must be positive or zero, and in fact $\mathrm{tr}(-\tau_p) = 0$ implies that $(-\tau_p)$ is identically equal to zero. Therefore, we can use $\mathrm{tr}(-\tau_p)$ as a local measure of the importance of the "elastic effects" in the flow. From a structural point of view, $\mathrm{tr}(-\tau_p)$ may be related to the local deviation from the equilibrium configuration of the polymer molecules. Thus if we take the single-mode Oldroyd-B model to represent a solution of Hookean elastic dumbbells,

$$\mathrm{tr}(-\tau_p) = 3\left(\frac{\langle Q^2\rangle}{\langle Q^2\rangle_{\mathrm{eq}}}-1\right)\int_0^{\infty} M(s)ds, \tag{18}$$

where $\langle Q^2\rangle$ and $\langle Q^2\rangle_{\mathrm{eq}}$ represent the mean square end-to-end distance of the dumbbells during flow and at equilibrium, respectively.

B. Discretization

We use the following finite element discretization for the particle positions at time t:

$$r = \sum_{j=1}^{N} r_j \phi^j, \tag{19}$$

$$z = \sum_{j=1}^{N} z_j \phi^j. \tag{20}$$

Here the (r_j,z_j) for $j = 1,2,...,N$ are the coordinates of node i at time t. The total number of nodes is N, and the ϕ^j are bilinear shape functions defined on a quadrilateral parent element. The shape functions are independent of time, so that the motion of all particles is specified by the vector functions $[r_j(t),z_j(t)]$. The velocity field at time t is then approximated as

$$v_z = \frac{z(t)-z(t-\Delta t)}{\Delta t},$$

$$v_r = \frac{r(t)-r(t-\Delta t)}{\Delta t},$$

and the acceleration field at time t as follows:

$$a_z = \frac{v_z(t)-v_z(t-\Delta t)}{\Delta t},$$

$$a_r = \frac{v_r(t)-v_r(t-\Delta t)}{\Delta t}.$$

The pressure field is approximated as

$$\mathscr{P} = \sum_{k=1}^{M} \mathscr{P}_k \psi^k, \tag{21}$$

where the $\mathscr{P}_k$ are nodal values, ψ^k shape functions, and M the number of pressure nodes.

The Galerkin forms of Eqs. (13) and (14) with ϕ^i as weight functions may be written

$$\int_V \left\{ \rho_f \frac{\partial^2 r}{\partial t^2} + \frac{1}{r}\frac{\partial}{\partial r}[r(\mathscr{P}+\tau_{rr})] + \frac{\partial}{\partial z}(\tau_{zr}) - \frac{\mathscr{P}+\tau_{\theta\theta}}{r} \right\} \phi^i r \, dr \, dz \, d\theta = 0, \quad (22)$$

$$\int_V \left[\rho_f \frac{\partial^2 z}{\partial t^2} + \frac{1}{r}\frac{\partial}{\partial r}(r\tau_{zr}) + \frac{\partial}{\partial z}(\mathscr{P}+\tau_{zz}) \right] \phi^i r \, dr \, dz \, d\theta = 0. \quad (23)$$

Here V is the domain of the fluid. By an integration with respect to θ followed by the use of the Gauss–Ostrogradskii theorem we find

$$-\int_\Gamma (\pi_r + \rho_f g z n_r)\phi^i r \, ds + \int_A \left(\rho_f r \frac{\partial^2 r}{\partial t^2}\phi^i + \mathscr{P}\frac{\partial \phi^i r}{\partial r} + r\tau_{rr}\frac{\partial \phi^i}{\partial r} + r\tau_{zr}\frac{\partial \phi^i}{\partial z} + \tau_{\theta\theta}\phi^i \right) dr \, dz = 0, \quad (24)$$

$$-\int_\Gamma (\pi_z + \rho_f g z n_z)\phi^i r \, ds + \int_A \left(\rho_f r \frac{\partial^2 z}{\partial t^2}\phi^i + \mathscr{P}\frac{\partial \phi^i r}{\partial z} + r\tau_{zr}\frac{\partial \phi^i}{\partial r} + r\tau_{zz}\frac{\partial \phi^i}{\partial z} \right) dr \, dz = 0. \quad (25)$$

Here A is the area of the fluid in the (r,z) plane, Γ designates the boundary, and s is an arc length along the boundary curve. Also (π_r,π_z) are the components of the force per unit area exerted by the fluid on the surroundings. Similarly (n_r,n_z) are the components of a unit vector normal to the boundary directed outwardly from the fluid.

C. Equation of motion for the sphere

We imagine an axisymmetric body located on the z axis. The force exerted by the fluid on this body may be evaluated by integrating the pressure and stresses over the body. Certainly the stress components may be obtained from Eq. (15). However, it is more accurate to invoke the z component of the equation of motion as follows. Note first that by definition the force in the axial direction F exerted by the fluid on the body is given by

$$F = \int_{A_s} \pi_z \, dA = 2\pi \int_{\Gamma_s} \pi_z r \, ds$$

$$= 2\pi \int_{\Gamma_s} \pi_z \sum_{i=1}^{L} \phi^i r \, ds = 2\pi \sum_{i=1}^{L} \int_{\Gamma_s} \pi_z \phi^i r \, ds. \quad (26)$$

Here A_s is the surface of the body, while Γ_s is the boundary of the body in the (r,z) plane. The ϕ^i are global shape functions associated with the nodes $i = 1,2,\ldots,L$ on Γ_s. Thus from Eq. (25) we obtain

$$F = 2\pi \sum_{i=1}^{L} \int_A \left(\rho_f r \frac{\partial^2 z}{\partial t^2} \phi^i + \mathscr{P} \frac{\partial \phi^i r}{\partial z} + r\tau_{zr} \frac{\partial \phi^i}{\partial r} + r\tau_{zz} \frac{\partial \phi^i}{\partial z} \right) dr\, dz$$

$$-2\pi \sum_{i=1}^{L} \int_\Gamma \rho_f g z n_z \phi^i r\, ds. \tag{27}$$

The domain of integration A consists of the elements adjacent to the axisymmetric body since the ϕ^i are zero outside that domain. The final term in Eq. (27) describes the buoyancy of the axisymmetric body. To show this we rewrite part of the term as an integral over the surface of the body,

$$I = 2\pi \sum_{i=1}^{L} \int_{\Gamma_s} z n_z \phi^i r\, ds = \int_{\Gamma_s} z n_z 2\pi r\, ds = \int_A z n_z\, dA, \tag{28}$$

where A is the surface of the body. We now introduce the unit vector $\mathbf{n}_s$ which is outward normal to the body. Then the integral may be evaluated as follows:

$$I = -\boldsymbol{\delta}_z \cdot \int_A z \mathbf{n}_s\, dA = -\boldsymbol{\delta}_z \cdot \int_V \nabla z\, dV = -\int_V dV = -V, \tag{29}$$

where V is the volume of the body. Hence the force exerted by the fluid on the body is given by

$$F = 2\pi \sum_{i=1}^{L} \int_A \left(\rho_f r \frac{\partial^2 z}{\partial t^2} \phi^i + \mathscr{P} \frac{\partial \phi^i r}{\partial z} + r\tau_{zr} \frac{\partial \phi^i}{\partial r} + r\tau_{zz} \frac{\partial \phi^i}{\partial z} \right) dr\, dz + \rho_f g V. \tag{30}$$

By using a discretization of the modified pressure $\mathscr{P}$ rather than the physical pressure p we obtain an exact determination of the buoyancy, which gives better accuracy in the determination of F.

The final equation of motion for the sphere becomes

$$\rho_s V \frac{d^2 z_s}{dt^2} = F - \rho_s g V. \tag{31}$$

Here z_s is a z coordinate of the sphere.

D. Time discretization

We have used two different schemes for discretization of the time integrals. The two methods differ in their time convergence where method 1 [described in Rasmussen and Hassager (1993) and used in the computations for the single-mode Oldroyd model here] has Δt convergence while method 2 (used in the computations for the multimode model here) has Δt^2 convergence.

Both methods can use variable time steps. For the heavy spheres (De > 2.45) the initial Δt is 0.001 s which is gradually increased to 0.005 s. For the lighter spheres the initial Δt is 0.0005 s (due to the steep gradient in velocity) and the time step is gradually increased to 0.01 s, since the overall deformation in the fluid is small. Convergence tests have been performed to check the convergence of the two schemes.

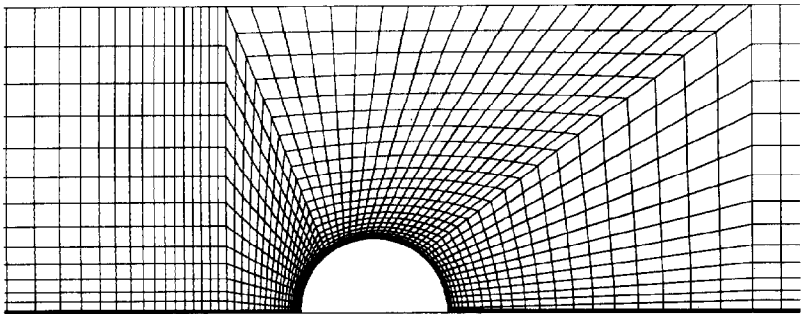

FIG. 6. Configuration of the finite element mesh with 1605 elements at time $t = 0$. Motion of the sphere is from left to right.

E. Geometry and boundary conditions

The simulations have been performed on the same geometry that is used in the experimental work and described in Sec. II B [see also Figs. 1(a) and 1(b)]. Thus the fluid is contained in a closed tube of length 90 cm and radius 5.23 cm. A centered sphere is released (from rest) at time $t = 0$ in a quiescent fluid with the center of the sphere 10 cm from the top of the tube.

The finest mesh used in the simulations has 1605 elements. The configuration of the mesh at time $t = 0$ is seen in Fig. 6. The mesh is deformed as a result of the motion of the sphere, and it is therefore necessary to introduce new meshes as described in Rasmussen and Hassager (1993).

In previous simulations (Rasmussen and Hassager, 1993) the spatial convergence of the method has been shown to be at least first order in the numbers of elements. Furthermore, it was demonstrated that a mesh with 1017 elements gave a maximum error in the determination of the relative force of 5.5×10^{-3}. Based on this investigation we expect the spatial discretization used here to give a maximum error in the determination of the relative force of 3.5×10^{-3}.

IV. RESULTS

The experimental transient velocity profile for a Delrin sphere at a Deborah number of De = 0.406 is shown in Fig. 7. The data shows a small overshoot followed by a monotonic approach at longer times to a steady-state value, denoted U_∞. This final velocity U_∞ is higher than the calculated value U_S, indicating a reduction in the drag compared to that expected in a Newtonian fluid. The gap in the data around time $t = 1.5$ s is a result of switching from the initial strategy of loading frames directly into memory to processing each individual frame before acquiring the subsequent frame, as described in Sec. II C. There is an unknown time delay associated with switching from one algorithm to the other, and so velocities cannot be calculated accurately in this transition region.

The velocity time series for each of the 2.54 cm diameter spheres are shown in Fig. 8. As the sphere density (and the Deborah number) increases, the ultimate steady-state velocity U_∞ of the sphere increases, as does the magnitude of the velocity overshoot. The same data are shown in normalized form in Fig. 9. The time is non-dimensionalized by the single-mode Oldroyd-B relaxation time λ_1 for the fluid, and the velocity is scaled by the equivalent Newtonian settling velocity U_S. This figure clearly

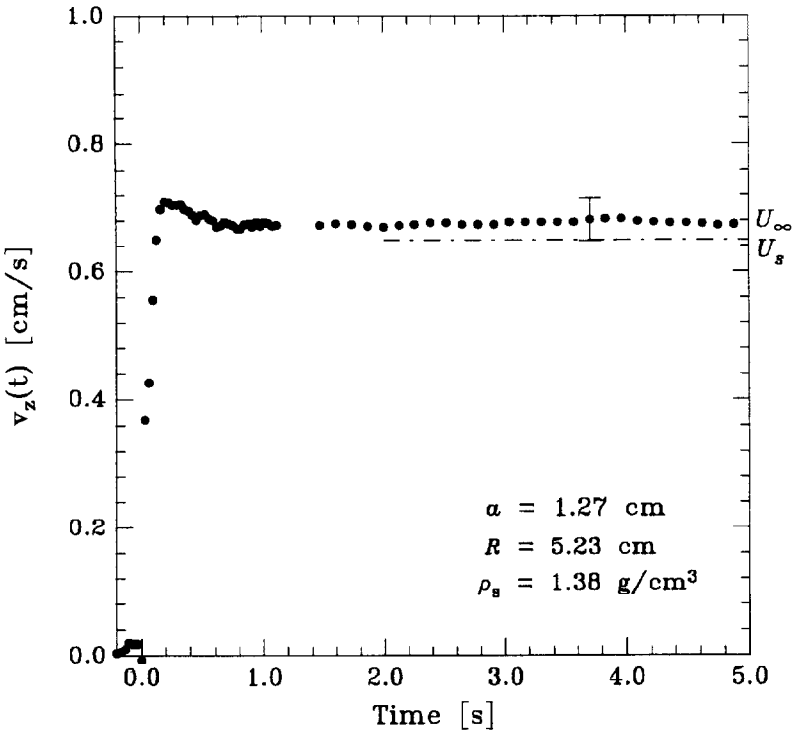

FIG. 7. Experimentally determined velocity profile for the Delrin sphere at a nominal Deborah number of De = 0.406. The broken line indicates the equivalent settling velocity U_s for an identical sphere in a tube of Newtonian fluid.

shows that U_∞ is a function of De; at low De the measurements indicate a drag decrease, followed by a drag increase at higher De. The relative size of the maximum velocity overshoot with respect to U_∞ also increases with De, reaching nearly 50% at our highest Deborah number of De = 11.7. Teflon spheres (De = 1.07) show small decaying oscillations following the overshoot, whereas all other cases indicate a monotonic decrease towards U_∞. Finally, it can also be discerned from a careful inspection of Fig. 9 that the temporal position of the maximum velocity also shifts to slightly longer times as the density and inertia of the sphere increases.

Transient numerical results from a 1-mode Oldroyd-B simulation for four values of De up to 3.347 are shown in Fig. 10. The results show the same qualitative behavior as obtained in the experiments, but with a much larger relative overshoot followed by a monotonic decay to steady state. While the inertia of the sphere and fluid is included in the simulations, it has in fact very little influence on the transient sphere velocity, except for very small times, due to the high value of the elasticity number. This means that the overshoot is a purely viscoelastic effect that may be considered as an analog of overshoot in creep experiments. The fluid simply needs a certain overall deformation, or equivalently a certain length of time at a given deformation rate, before the elastic stresses build up. In fact, for the single-mode Oldroyd-B model the maximum velocity $U_{\max}$ may be estimated by assuming that the elastic term does not contribute anything to the stress, and that at short times, $\rho_f a^2/n_0 \ll t \ll \lambda_1$, the sphere is in

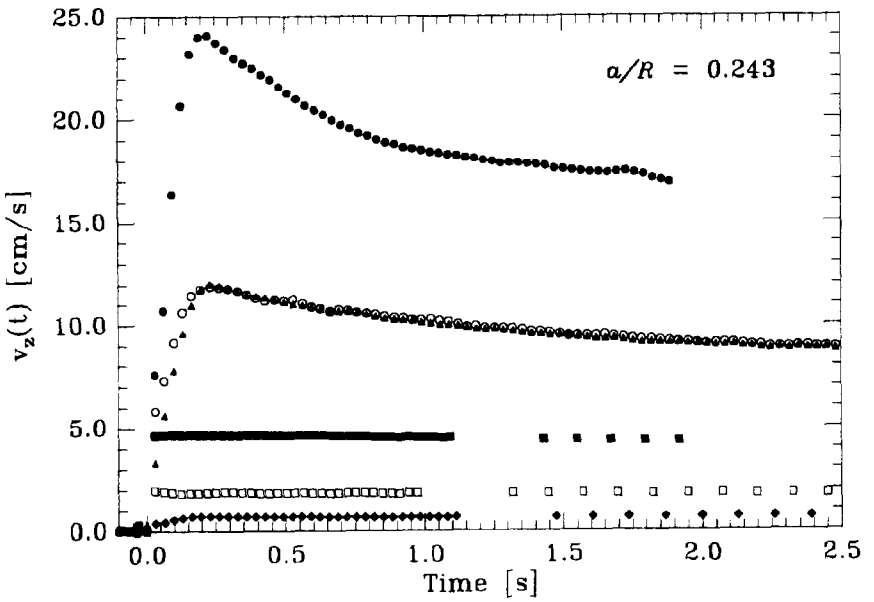

FIG. 8. Experimentally determined velocity profiles for spheres accelerating under gravity in the PIB/PB/C14 Boger fluid. (◆) Delrin sphere, De = 0.406; (□) Teflon sphere, De = 1.07; (■) ceramic sphere, De = 2.45; (▲) bronze sphere, De = 5.53 (○) chrome sphere, De = 5.73; (●) tungsten carbide sphere, De = 11.7.

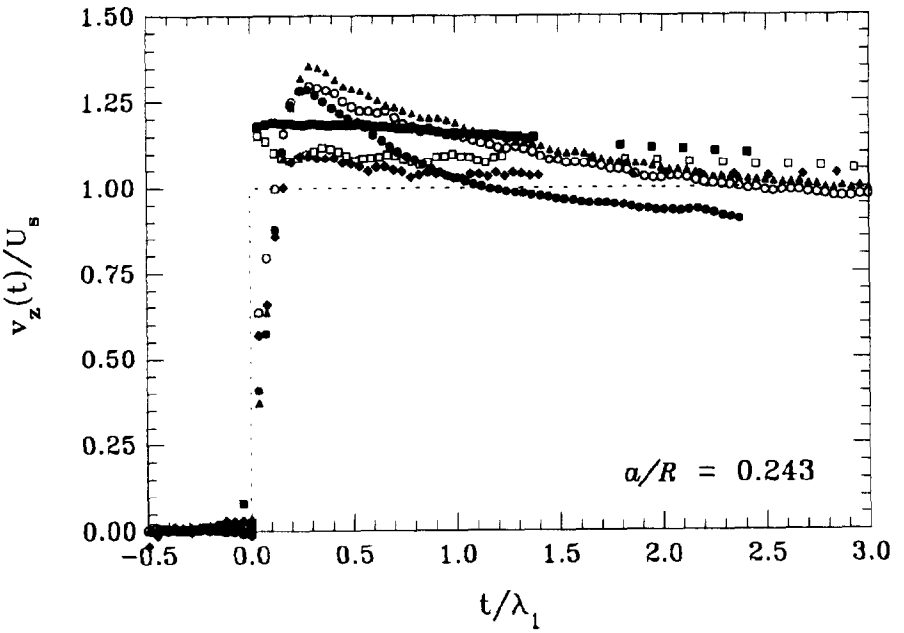

FIG. 9. Velocity profiles normalized with the steady-state velocity U_s expected for a sphere of same size and density falling through a Newtonian fluid of equivalent viscosity and density to the PIB Boger fluid. Symbols and flow conditions are identical to those given in Fig. 8.

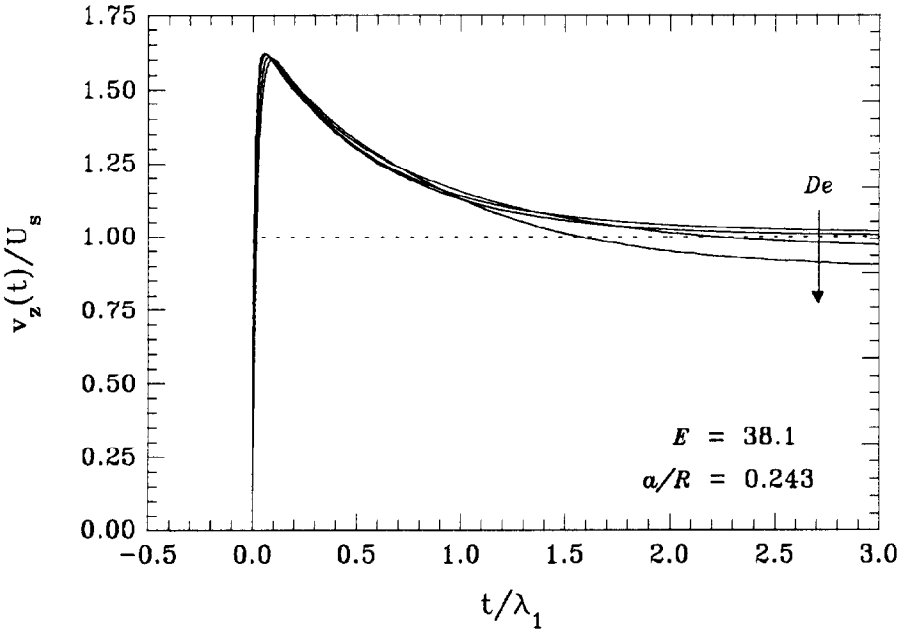

FIG. 10. Normalized results of numerical simulations with the Oldroyd-B model for the transient motion of a sphere in a tube as the Deborah number is increased from De = 0.402 to De = 3.81. The dashed line indicates the Newtonian settling velocity U_s.

free-fall through a fluid with an instantaneous viscosity η_s arising from the solvent only. This gives the following estimate at large values of the elasticity number:

$$U_{\max}/U_0 \simeq \eta_0/\eta_s = 1.69. \tag{32}$$

Figure 10 shows that Eq. (32) gives a reasonable estimate of the maximum velocity for all Deborah numbers investigated. Note also that the dependence on Deborah number is not very strong, when the data are reduced as in Fig. 10. In fact, as we note in Sec. V, for De $\to$ 0 the curves approach a limiting behavior that corresponds to linear viscoelasticity.

The steady-state drag behavior is given in Fig. 11, where we plot the dimensionless drag coefficient defined in Eq. (7) as a function of the actual Deborah number De_1 based on the ultimate velocity U_∞ in the viscoelastic test fluid. This allows more convenient comparison between numerical solutions and experimental data at steady-state conditions. The solid line represents the numerical results, while the individual squares are experimental steady-state data (with error bars) obtained from the experimental technique described above, as well as via visually timing the fall speed. The experiments and the simulations show the same qualitative dependence on the Deborah number: At low Deborah numbers a small decrease in the drag coefficient, followed by a larger increase at high Deborah numbers. Furthermore, the simulations do seem to fall roughly within the uncertainty estimated for the experiments, thus indicating that the Oldroyd-B model gives a reasonable prediction of the steady drag up to an actual Deborah number of about 3.3. The simulations could not be carried through to steady state for $De_1 > 3.347$ due to loss of numerical convergence.

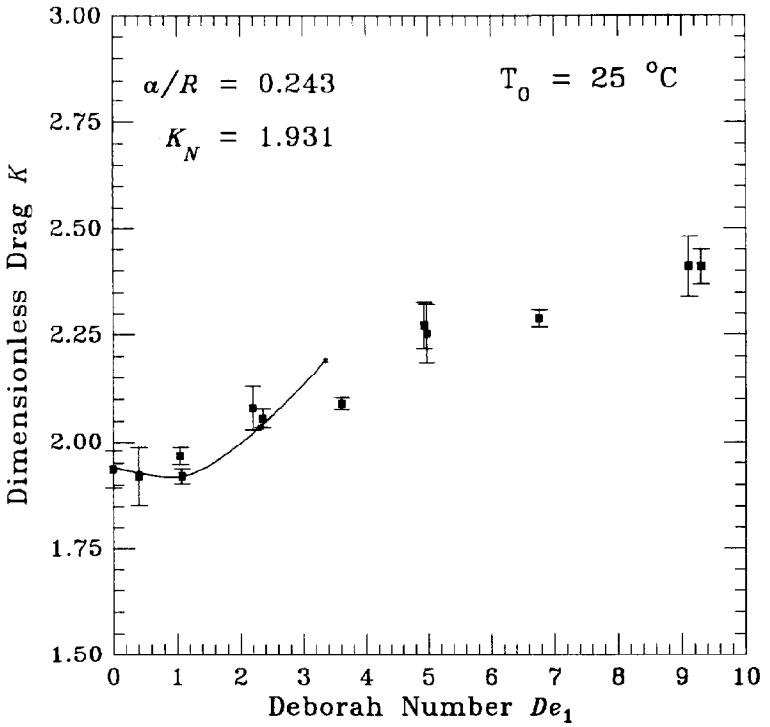

FIG. 11. The dimensionless drag correction factor $K(\kappa,\mathrm{De})$ as a function of the actual Deborah number in the flow, De_1, based on the Oldroyd-B relaxation time λ_1, and the actual steady settling velocity U_∞. (■) Experimental measurements with error bars ($\pm 2\sigma$); (– –) Oldroyd-B numerical simulations.

At our highest Deborah number of $\mathrm{De}_1 = 9.3$, the dimensionless drag is $K = 2.4$, representing a 24% drag increase. The steady-state drag force for a sphere in creeping motion has previously been measured experimentally by Tirtaatmadja *et al.* (1990) in the M1 Boger fluid and by Chmielewski *et al.* (1990) in corn syrup-based and polybutene-based Boger fluids. Both give the dimensionless drag coefficient X_e for spheres settling in unbounded domains, the former showing a drag increase of nearly 30% at a Deborah number $\mathrm{De} \sim 2$, while the latter found a drag increase of about 15% at $\mathrm{De} \sim 0.7$ in a PIB fluid, but a drag reduction of about 25% in corn syrup-based fluids.

An appreciation of the numerical difficulties in the simulations of the steady motion in the Oldroyd-B fluid may be obtained from Figs. 12(a) and 12(b), where we plot $\mathrm{tr}(-\tau_p)$, normalized by $\int_0^\infty M(s)ds = (\eta_0-\eta_s)/\lambda_1$, for $\mathrm{De}_1 = 2.31$ ($\mathrm{De} = 2.45$) at $t/\lambda_1 = 5.0$. In Fig. 12(a), a large wake of stretched polymers extending more than eight sphere radii downstream is clearly visible. The qualitative features of this plot are very similar to those found by Chilcott and Rallison (1988). We believe the calculated drag increase results from the increase in the effective size of the sphere due to this highly extended polymer region. The maximum is located approximately $0.5a$ behind the aft stagnation point of the sphere. The normalized values of $\mathrm{tr}(-\tau_p)$ at the two stagnation points are below 0.1. We believe this indicates a value of 0 (within numerical accuracy) at the stagnation points in agreement with Chilcott and Rallison. The numerical difficulties are probably related to the very steep gradient in $\mathrm{tr}(-\tau_p)$ where

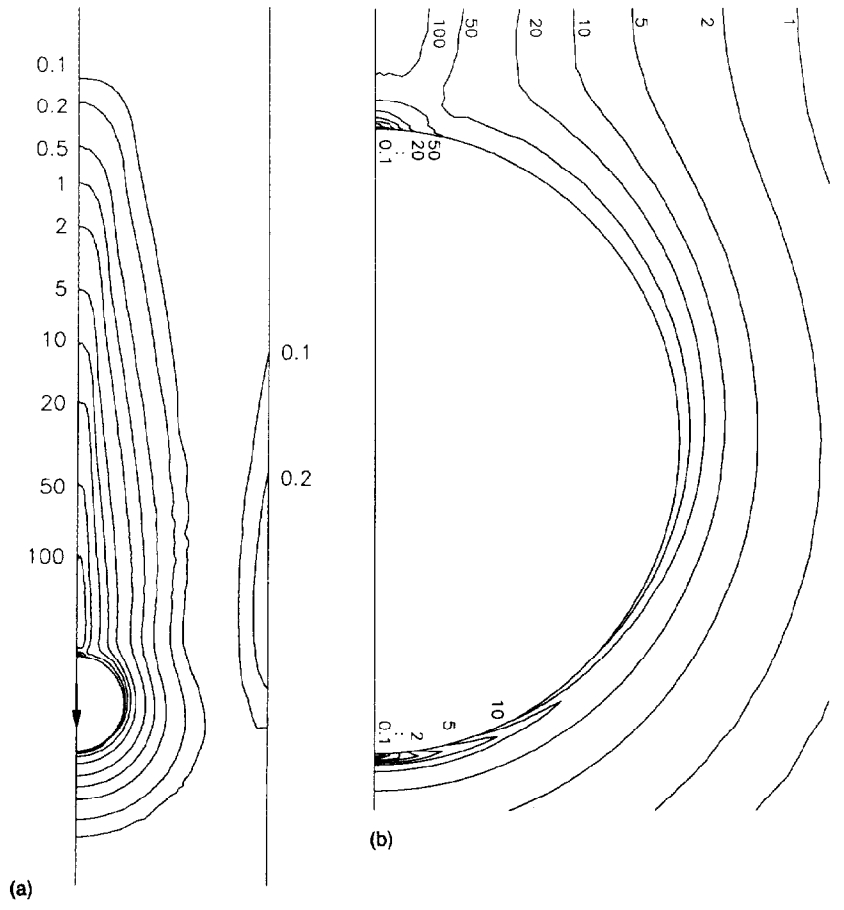

FIG. 12. (a) Contours of the dimensionless trace of the polymeric contribution to the stress tensor $\mathrm{tr}[-\tau_p\lambda_1/(\eta_0-\eta_s)]$ representing the total extension of the polymer molecules in the fluid at De = 2.45 and $t/\lambda_1 = 5.0$. (b) Magnification of the steep boundary layers in $\mathrm{tr}(-\tau_p)$ near the forward and aft stagnation points of the sphere.

we have simulated an increase by a factor of 10^3 over half a radius. Clearly a very high mesh resolution is required to resolve such gradients. Similar stress boundary layers and numerical convergence limits have recently been discussed by Lunsmann *et al.* (1993).

A better appreciation of the details near the sphere is obtained from Fig. 12(b). In particular, the low values near the actual stagnation points are more clearly visible. In addition we may identify three regions with different contributions to $\mathrm{tr}(-\tau_p)$: a region near the front stagnation point with biaxial stretching, a region with shearing over most of the sphere, and a region of uniaxial stretching in the wake near the aft stagnation point, as first discussed by Chilcott and Rallison.

In Figs. 13(a) through 13(c), we compare the experimental results with results obtained from numerical simulations using both one-mode and four-mode Oldroyd-B models for Deborah numbers of De = 0.407, 5.73, and 11.7, respectively. In these

figures, we show both the dimensional velocity and time on the left-hand and lower axes, and the equivalent dimensionless quantities v_z/U_s and t/λ_1 on the right-hand and upper axes, respectively. The results show that the multimode model provides greatly improved quantitative agreement with experimental data over the single-mode calculations, reducing the magnitude of the overshoot and modifying long time scale behavior. In the multimode models, the decay in velocity following the overshoot is initially dominated by the shorter of the time constants in the spectrum λ_i, resulting in a steeper slope and faster decay to the asymptotic value than for the single-mode Oldroyd-B model. However, at longer times, the effects of the shorter time constants die away, leaving only the largest time constant to influence the long-time asymptote towards steady state. This results in a decreased slope and slower decay than for the single-mode Oldroyd-B predictions.

The agreement between the experimental data and the multimode simulations is best at high De, and worst at low De. In the numerical calculations, as the Deborah number goes to zero, there will still be an overshoot in velocity corresponding to the linear viscoelastic limit. The experimental data, however, seem to suggest that the amplitude of the overshoot almost disappears at lower De. We are not able to resolve the discrepancy at low De at the present time. However, the lightest spheres fall away from the release mechanism far more slowly than the dense spheres, and the initial experimental conditions therefore more closely represent the numerical initial conditions at high De.

V. DISCUSSIONS AND CONCLUSIONS

A digital imaging system has been used to obtain the first quantitative experimental data on the transient behavior of a sphere falling from rest through a PIB Boger fluid along the center line of a cylindrical tube. Velocity overshoots of up to 50% have been observed at high De confirming earlier theoretical and numerical predictions. Our numerical simulations with the Oldroyd-B constitutive model demonstrate the correct qualitative behavior, but fail to accurately describe the magnitude of the overshoot or the slow approach to steady state at long times. An almost quantitative agreement between experiments and computations has been achieved by extending the calculations to a multimode formulation of the Oldroyd-B model which captures, at least approximately, the spectrum of relaxation times present in a real Boger fluid. Converged numerical solutions were obtained using the Lagrangian finite element technique up to De = 3.35. At higher Deborah numbers, we were not able to obtain values of the ultimate steady-state settling velocity U_∞, due to the loss of spatial numerical convergence in the large viscoelastic stresses and velocity gradients that develop. However, we were able to obtain temporally converged solutions of the initial transient velocity of the sphere at high De.

Our measurements of the wall correction factor K for steady viscoelastic flow of a sphere in a tube corroborate the earlier findings of Tirtaatmadja *et al.* (1990) and Chmielewski *et al.* (1990) of a pronounced drag increase in PIB-based Boger fluids at high De. By obtaining measurements of U_∞ in tubes of differing cross section, it is possible to calculate the viscoelastic drag correction factor X_e in the absence of bounding walls. These measurements will be reported on at a later date, but show the same general trend as the data in Fig. 11. The predictions of the Oldroyd-B model provide good agreement with the experimental values of K up to the maximum Deborah number before loss of numerical convergence. At higher De, it appears that the actual drag increase is less than that predicted by the Oldroyd-B model. This more gradual

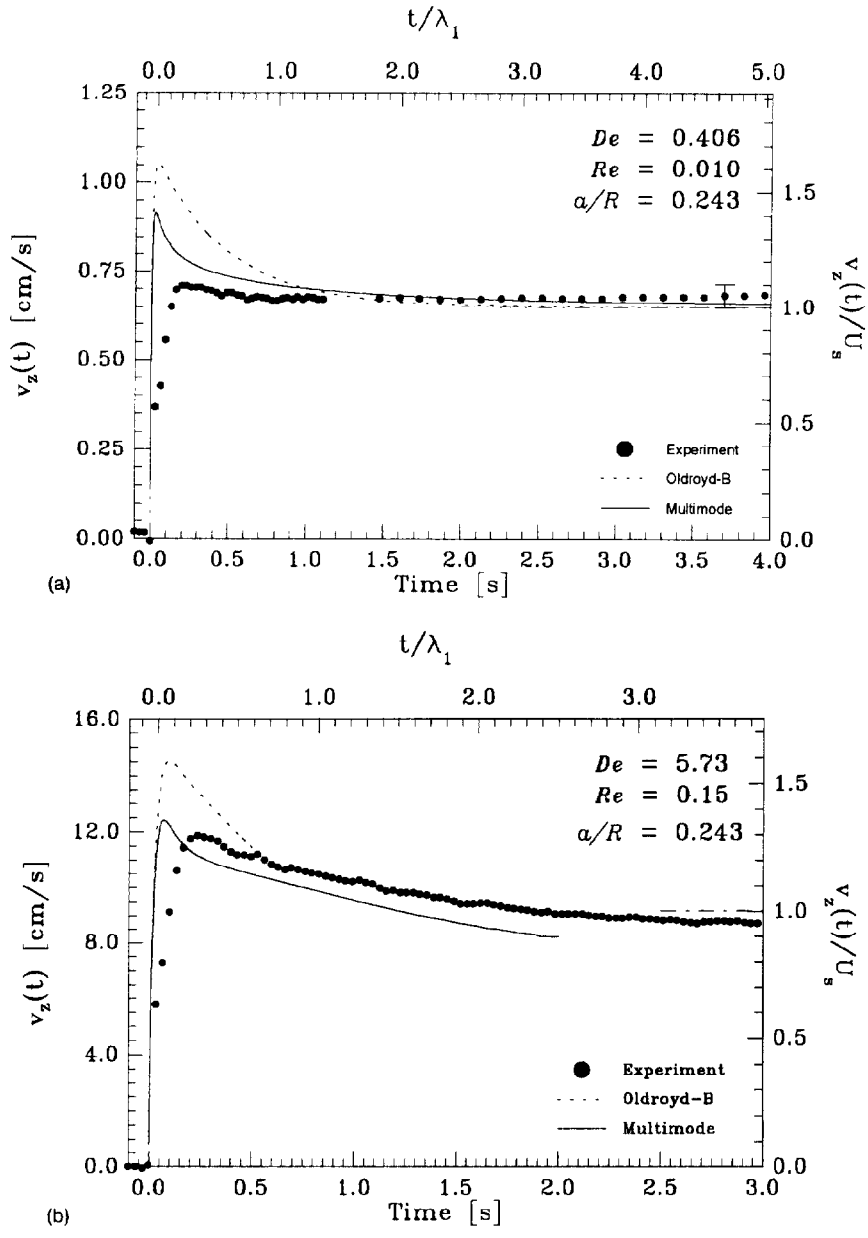

FIG. 13. (a) Comparison of experimental measurements (●) and computations using the Oldroyd-B model (- - -) and multimode model (—) for Delrin spheres, De = 0.406; Re = 0.010. (b) Comparison of experimental measurements (○) and computations using the Oldroyd-B model (- - -) and multimode model (—) for chrome spheres, De = 5.73, Re = 0.15. (c) Comparison of experimental measurements and numerical computations using the Oldroyd-B model (- - -) and the multimode model (—) for tungsten carbide spheres at flow conditions of De = 11.7, Re = 0.31.

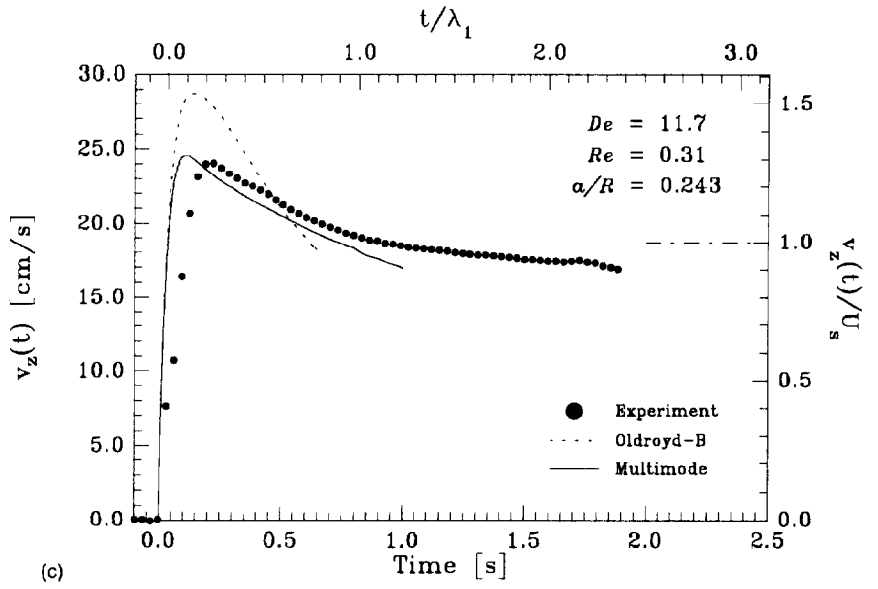

FIG. 13. (*Continued.*)

increase in K with De is due to the pronounced shear thinning in the elastic property $\Psi_1(\dot{\gamma})$ observed for real Boger fluids (Quinzani *et al.*, 1990). The large values of Deborah number shown in the experimental data of Fig. 11 arise because our definitions of De and De_1 are based on the zero-shear-rate relaxation time λ_1. The actual magnitudes of elastic effects in a flow at high shear rates are better estimated by the use of a shear-rate-dependent relaxation time $\lambda_1(\dot{\gamma})$, calculated from the actual viscometric data for the Boger fluid. Using this definition and the highest nominal shear rate (U_∞/a) for the tungsten carbide sphere yields a relaxation time of $\lambda_1(\dot{\gamma}) = 0.35$ s at a shear rate of 12.0 s^{-1} corresponding to a shear-rate-dependent Deborah number $De_1(\dot{\gamma}) = 4.25$. Although this is a more realistic estimate of elastic effects in the flow, it makes comparison with numerical calculations difficult, and it is better to use λ_1 to define the Deborah number, and to introduce a constitutive equation capable of explicitly capturing shear thinning in $\Psi_1(\dot{\gamma})$.

Recent steady-state calculations by Lunsmann *et al.* (1993) for spheres settling in tubes with radius ratios of $\kappa = 0.5$ and $\kappa = 0.125$ have been able to model this phenomenon by using single-mode constitutive models which capture the nonlinear fluid rheology of Boger fluids at high shear rates. In this work, the authors used the nonlinear model of Chilcott and Rallison (1988), and varied the extensibility parameter L, which controls the shear thinning in $\Psi_1(\dot{\gamma})$ and the increase in extensional viscosity $\bar{\eta}(\dot{\epsilon})$ predicted by the model. For low values of $L \leqslant 5$, the authors predicted a monotonic decrease in the wall correction factor K with De in accordance with experimental observations with polyacrylamide Boger fluids (Chhabra *et al.*, 1980). For larger values of L, the calculations predicted an increase in the wall factor at high De with the curve asymptotically approaching the predictions of the Oldroyd-B model as $L \to \infty$. Recent attempts to use the Chilcott–Rallison model to compute steady viscoelastic flow of this 0.31 wt. % PIB Boger fluid past a cylinder in a channel (McKinley *et al.*, 1993) have suggested that the fluid is modeled by a value of $L = 12$.

From the computations of Lunsmann *et al.* we should thus expect an increase in K at high De, but of a magnitude lower than that predicted with the Oldroyd-B model, just as observed in our experiments. Lunsmann *et al.* also report related benefits of using a model with finite extensibility are that the severity of the velocity gradients near the sphere is greatly reduced, and that the computations can be carried out without apparent upper limit in De. Calculations of K with the Chilcott–Rallison model for this fluid are currently underway. Of course, it is worth noting that quantitative simulations of both the transient velocity of the sphere at intermediate times and its asymptotic drag increase at high De and long times really require incorporation of both a spectrum of time constants and nonlinear fluid rheology.

The early theoretical work by King and Waters (1972) and later numerical work of Zheng and Phan-Thien (1992) showed that by observing the transient velocity of a sphere in a viscoelastic fluid, it is possible to obtain information about the rheological response of a viscoelastic fluid in a nonhomogeneous shear flow. In particular, both sets of authors showed that the magnitude of the maximum velocity $U_{\max}$ and the temporal location of this overshoot both scale closely with $\sqrt{\lambda_1}$. For a series of experiments with spheres of differing density ρ_s in a single fluid with a fixed elasticity number, it is not possible to verify this prediction. However, it is still possible to use our data to obtain insight into the nonlinear viscoelastic effects in this nonhomogeneous flow. In Sec. IV, we have already remarked on the similarity of this nonhomogeneous flow to a simple creep experiment in linear viscoelasticity, at least for short times and small strains. At longer times and larger strains, nonlinear elastic effects become important, and curves of sphere displacement vs time resemble nonlinear viscoelastic creep curves. In Fig. 14(a) we show a plot of the experimental position vs time data for chrome steel and tungsten carbide spheres. The two dashed lines are drawn tangent to each position profile at long times, with slopes based on the corresponding measured value of U_∞. The intercept of these dashed lines with the abscissa is -0.52 s for chrome steel and -0.49 s for tungsten carbide. This offset will in general depend on the spectrum of time constants as well as the relative inertia of the sphere to the fluid, but it gives some measure of the retardation processes in this inhomogeneous flow, and is remarkably close to the estimate of $\lambda_2 = \beta\lambda_1 = 0.48$ s calculated from the Oldroyd-B model.

Second, it is possible to get an estimate of the longest relaxation processes in the fluid by observing the decay in the velocity overshoot at long times. In Fig. 14(b), we plot on a semilogarithmic scale the deviation $[v_z(t_i) - U_\infty]$ from the ultimate steady-state value for chrome steel and tungsten carbide spheres, and the data approaches a straight line of slope -0.839 s^{-1} for chrome steel and -0.630 s^{-1} for tungsten carbide. This represents an exponential decay at long times with time constants for each case given by the negative of the inverses of the above slopes, yielding values of 1.19 and 1.59 s for chrome steel and tungsten carbide, respectively.

The most pronounced discrepancy between our experimental observations and numerical calculations occurs with our least dense spheres at the lowest Deborah numbers. The numerical calculations presented in Fig. 10 show that the magnitude of the predicted velocity overshoot does not decrease with decreasing De. In fact, for a fixed value of the elasticity number $E \gg 1$, the large unvarying transient response as De $\to 0$ represents the linear viscoelastic response of the Oldroyd-B model to an instantaneously applied constant gravitational body force on the sphere. The velocity overshoot only decreases to zero as the elasticity number, representing the ratio of the elastic to the viscous time scales in the flow, decreases to $E \leqslant 1$. The simplest one-dimensional calculations of startup of steady shearing flow under imposition of a

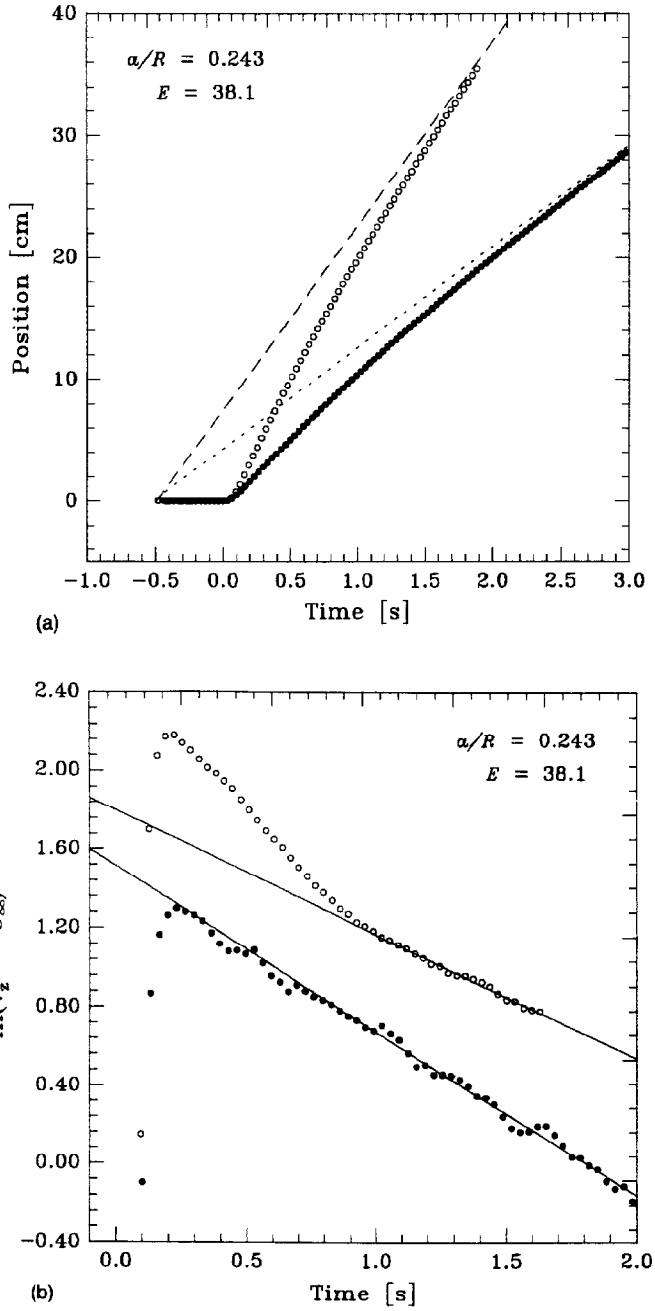

FIG. 14. (a) Estimate of the characteristic time scale for retardation processes in the nonhomogeneous flow from Lagrangian position data for nominal flow conditions of De = 5.72 (●) and De = 11.7 (○). (b) Estimate of the longest relaxation time from measurements of the decay of the velocity overshoot $[v_z(t) - U_\infty]$ at long times for De = 5.72 (●) and for De = 11.7 (○).

constant *stress* show a similar effect, and, as noted earlier, the magnitude of the initial overshoot in shear rate for such a calculation is in good agreement with our calculations shown in Fig. 10. Although the influence of our release mechanism and associated experimental errors will be largest for the slowest moving spheres, our experimental measurements at low De not show even the same qualitative behavior as the Oldroyd-B computations, and it appears clear that the relatively large value of the elastic contribution η_p in the Oldroyd-B model fit does not accurately represent the predominantly viscous transient response of our Boger fluid at low De. The situation is substantially improved by using a multimode model, which better represents the more rapid increase in the total viscous stresses acting on the sphere.

It is clear from these results that this relatively simple inhomogeneous flow is an excellent benchmark problem for probing transient phenomena in viscoelastic liquids, and for rigorously verifying the predictions of numerical simulations. In particular, our results highlight the inadequacies of the single-mode Oldroyd-B model in predicting transient flows of Boger fluids even at low De.

ACKNOWLEDGMENTS

L. E. B. and G. H. M. would like to thank the National Science Foundation for the financial support of this work, as well as Ms. Nina Shapley, Mr. Jean Moreau, and Mr. Michael T. Kezirian for their assistance with some of the experimental measurements. H. K. R. and O. H. would like to thank the Danish Technical Research Council for their financial support of this work (Grant No. 16-4927-1 PG). The band LU decomposition subroutines used in this work were developed by Dr. Peter Henriksen.

References

Bird, R. B., R. C. Armstrong, and O. Hassager, *Dynamics of Polymeric Liquids* (Wiley, New York, 1987), Vol. 1.

Ch. Bodart and M. J. Crochet, "Time-Dependent Viscoelastic Flow Around a Sphere," Presentation at the 64th Society of Rheology Conference, Santa Barbara, Feb. 1993.

Chhabra, R. P., *Bubbles, Drops, and Particles in Non-Newtonian Fluids* (Chemical Rubber, Boca Raton, 1992).

Chhabra, R. P. and P. H. T. Uhlherr, "The Influence of Fluid Elasticity on Wall Effects for Creeping Sphere Motion in Cylindrical Tubes," Can. J. Chem. Eng. **66**, 154–157 (1988).

Chhabra, R. P., P. H. T. Uhlherr, and D. V. Boger, "The Influence of Fluid Elasticity on the Drag Coefficient for Creeping Flow Around a Sphere," J. Non-Newt. Fluid Mech. **6**, 187–199 (1980).

Chilcott, M. D. and J. M. Rallison, "Creeping Flow of Dilute Polymer Solutions Past Cylinders and Spheres," J. Non-Newt. Fluid Mech. **29**, 381–432 (1988).

Chmielewski, C., K. L. Nichols, and K. Jayaraman, "A Comparison of the Drag Coefficients of Spheres Translating in Corn Syrup-Based and Polybutene-Based Boger fluids," J. Non-Newt. Fluid Mech. **35**, 37–49 (1990).

Ch, Y. I., J. P. Hartnett and E. Y. Kwack, "Study of Wall Effects for Viscoelastic Fluids in Falling Ball Viscometer," Chem. Eng. Commun. **6**, 141–149 (1980).

Cho, Y. I., J. P. Hartnett, and W. Y. Lee, "Non-Newtonian Viscosity Measurements in the Intermediate Shear Rate Range with the Falling Ball Viscometer," J. Non-Newt. Fluid Mech. **15**, 61–75 (1984).

Cygan, D. A. and B. Caswell, "Precision Falling Sphere Viscometry," Trans. Soc. Rheol. **15**, 663–683 (1971).

DeMestre, N. J. and D. F. Katz, "Stokes Flow About a Sphere Attached to a Slender Body," J. Fluid Mech. **64**, 817–826 (1974).

Happel, J. and H. Brenner, *Low Reynolds Number Hydrodynamics* (Martinus Nijhoff, Dordrecht, 1983).

Hassager, O., "Working Group on Numerical Techniques," J. Non-Newt. Fluid Mech. **29**, 2–5 (1988).

King, M. J. and N. D. Waters, "The Unsteady Motion of a Sphere in an Elastico-Viscous Liquid," J. Phys. D **5**, 141–150 (1972).

Lai, R. Y. S., "Drag on a Sphere Accelerating Rectilinearly in a Maxwell Fluid," Int. J. Engng. Sci. **12**, 645–655 (1974).

Lai, R. Y. S. and C. P. Fan, "Drag on a Sphere Accelerating Rectilinearly in an Elastico-Viscous Fluid," Int. J. Engng. Sci. **16**, 303–311 (1978).

Lunsmann, W. J., L. Genieser, R. A. Brown, and R. C. Armstrong, "Finite Element Analysis of Steady Viscoelastic Flow Around a Sphere: Calculations with Constant Viscosity Models," J. Non-Newt. Fluid Mech. **48**, 63–99 (1993).

Lamb, H., *Hydrodynamics* (Dover, New York, 1945).

McKinley, G. H., R. C. Armstrong, and R. A. Brown, "The Wake Instability in Viscoelastic Flow Past Confined Circular Cylinders," Philos. Trans. R. Soc. London **A344**, 265–304 (1993).

Mena, B., O. Manero, and L. G. Leal, "The Influence of Rheological Properties on the Slow Flow Past Spheres," J. Non-Newt. Fluid Mech. **26**, 247–275 (1987).

Quinzani, L. M., G. H. McKinley, R. A. Brown, and R. C. Armstrong, "Modeling the Rheology of Polyisobutylene Solutions," J. Rheol. **34**, 705–748 (1990).

Ramkissoon, H. and H. Shifang, "Unsteady Motion of a Sphere in an Elastico-Viscous Fluid," Int. J. Engng. Sci. **31**, 19–26 (1993).

Rasmussen, H. and O. Hassager, "Simulation of Transient Viscoelastic Flow," J. Non-Newt. Fluid Mech. **46**, 289–305 (1993).

Tirtaatmadja, V., P. H. T. Uhlherr, and T. Sridhar, "Creeping Motion of Spheres in Fluid M1," J. Non-Newt. Fluid Mech. **35**, 327–337 (1990).

Walters, K. and R. I. Tanner, "The Motion of a Sphere Through an Elastic Liquid," *Transport Processes in Bubbles, Drops, and Particles*, edited by R. P. Chhabra and D. DeKee (Hemisphere, New York, 1992).

Whitaker, S. and R. L. Pigford, "Numerical Differentiation of Experimental Data," Ind. Eng. Chem. **52**, 185–187 (1960).

Zheng, R. and N. Phan-Thien, "A Boundary Element Simulation of the Unsteady Motion of a Sphere in a Cylindrical Tube Containing a Viscoelastic Fluid," Rheol. Acta **31**, 323–332 (1992).